ON THE DESIGN OF NON-CONFORMING HIGH-RESOLUTION FINITE ELEMENT SCHEMES

Matthias Möller[1]

[1]Institute of Applied Mathematics (LS III)
TU Dortmund University of Technology, Vogelpothsweg 87, 44227 Dortmund, Germany
e-mail: matthias.moeller@math.tu-dortmund.de

Keywords: non-conforming finite elements, high-resolution schemes, convection-dominated flows, flux-corrected transport

Abstract. *The algebraic flux-correction (AFC) approach introduced in [8, 17] for the accurate treatment of convection-dominated flow problems and refined in a series of publications [9, 11–15, 18, 19] is extended to non-conforming finite element discretizations. Originally, this class of multidimensional high-resolution schemes was developed in the framework of conforming (multi-)linear P_1/Q_1 approximations. The underlying design criteria are revisited for non-conforming approximations on unstructured quadrilateral meshes. The properties of (non-)parametric rotated multi-linear Q_1^{rot} finite elements [23] are analyzed. The midpoint-value based variant $Q_1^{\mathrm{rot,MP}}$ is shown to violate essential design criteria unconditionally. The alternative definition of local basis functions in terms of integral mean values is shown to comply with the concepts of algebraic flux correction. A high-resolution continuous Galerkin scheme for $Q_1^{\mathrm{rot,MV}}$ finite elements is presented and investigated numerically for a two-dimensional benchmark problem with known exact solution. The advantages of the proposed non-conforming approach over P_1/Q_1 approximations are discussed. The regular structure of system matrices is the basis for using efficient sparse matrix formats such as ELLPACK on fully unstructured meshes. Further implementation details including aspects of parallelization are adressed.*

1 INTRODUCTION

The computation of non-oscillatory accurate solutions to convection-dominated problems is an important issue in numerical flow simulation. An algebraic approach to construct high-resolution schemes was introduced by Kuzmin [8]. It is based on a rigorous analysis of matrix properties that must be fulfilled by numerical methods to preserve positivity of physical quantities. In general, the Galerkin method does not satisfy these criteria. Strategies to enforce these constraints by adjusting matrix coefficients *a posteriori* have been proposed for linear and multi-linear finite element approximations [8, 9, 11–15, 17–19]. This technique is termed algebraic flux correction (AFC) and it can be used to turn a large number of unstable (low-order) discretizations into high-resolution schemes for convection-dominated flows. The extension of AFC schemes to higher-order finite elements was found to be possible but very challenging [10].

In the present paper, we apply the algebraic flux correction paradigm to non-conforming low-order finite element approximations on quadrilateral meshes. In particular, rotated multi-linear finite element spaces introduced by Rannacher and Turek in [23] for the solution of Stokes and Navier-Stokes equations are considered. They represent a natural generalization of the Crouzeix-Raviart element on simplices [2] to quadrilateral and hexahedral cells. The degrees of freedom are associated with the edges/faces which reduces continuity across element boundaries to a single point. In this respect, non-conforming elements seem to be more flexible in representing steep fronts and non-smooth solutions than their conforming counterparts.

A comprehensive review of the algebraic flux correction paradigm is given in [12, 13, 15]. The basic concepts of AFC schemes are summarized in Sections 2–3 and Appendix A. The aim is to outline the design criteria and algorithmic components that need to be validated for non-conforming finite elements. The design of finite element spaces is addressed in Section 4. It turns out that the definition of non-conforming local shape functions in terms of solution values at edge/face midpoints is not to be recommended in the context of algebraic flux correction. Some coefficients of the consistent mass matrix are unconditionally negative. Hence, application of row-sum mass lumping and the selective removal of mass diffusion by flux correction is questionable. These are essential steps of algebraic flux correction. Our numerical studies demonstrate that this approach towards non-conforming high-resolution schemes is impractical.

It is also possible to construct non-conforming finite elements by considering the mean values of the solution along edges/faces in integral sense. In this case, the coefficients of the consistent mass matrix are positive. Numerical benchmark computations confirm that algebraic flux correction concepts can be used without modification to turn a continuous Galerkin non-conforming Q_1^{rot} finite element approximation into a non-oscillatory high-resolution method.

It turns out that the use of non-conforming elements is beneficial for high performance and parallel computing. The coupling of degrees of freedom takes place over edges/faces, and therefore, the number of non-zero matrix entries per row is the same for all interior and boundary nodes, respectively. Structured sparse matrix formats are used to achieve optimal performance on modern hardware platforms for fully unstructured high-resolution finite element methods.

2 GALERKIN FEM APPROXIMATION

Consider the convective transport of the scalar quantity u by the externally given velocity field $\mathbf{v} = \mathbf{v}(\mathbf{x}, t)$ in the bounded domain $\Omega \subset \mathbb{R}^d$. Here, $d = 2, 3$ denotes the number of spatial dimensions. The model problem is governed by the unsteady convection equation

$$\frac{\partial u}{\partial t} + \nabla \cdot (\mathbf{v}u) = 0 \qquad \text{in } \Omega \tag{1}$$

which is of hyperbolic type. Thus, no boundary conditions are prescribed at the outflow part of the boundary $\Gamma = \partial\Omega$, whereas Dirichlet boundary conditions are imposed on the inflow part:

$$u = g \qquad \text{on } \Gamma_- := \{\mathbf{x} \in \Gamma \,:\, \mathbf{v} \cdot \mathbf{n} < 0\}. \tag{2}$$

Here, $\mathbf{n}$ denotes the outward unit normal vector to Γ. The problem statement is complemented by prescribing the initial profile $u(\mathbf{x}, t_0) = u_0(\mathbf{x})$ in the domain Ω at the initial time t_0.

The variational form of problem (1) reads: Find a solution $u \in \mathcal{V}$ such that

$$\int_\Omega w \left[\frac{\partial u}{\partial t} + \nabla \cdot (\mathbf{v}u) \right] \mathrm{d}\mathbf{x} = 0, \qquad \text{for all } w \in \mathcal{W}, \tag{3}$$

where $\mathcal{W}$ denotes the space of admissible test functions w vanishing on the Dirichlet part of the boundary Γ_-. Here, we abstain from giving a formal definition of Sobolev spaces $\mathcal{V}$ and $\mathcal{W}$.

A common practice in computing approximate solutions $u_h \approx u$ to conservation laws is to adopt Fletcher's group finite element formulation [4]. Given the time dependent coefficients

$$u_j(t) = u(\mathbf{x}_j, t) \qquad \text{and} \qquad \mathbf{v}_j(t) = \mathbf{v}(\mathbf{x}_j, t) \tag{4}$$

at the degrees of freedom $\mathbf{x}_j$ (to be defined in Section 4), the same finite set of basis functions $\{\varphi_j\}_{j=1}^{N_{\mathrm{dof}}}$ is used to interpolate the unknown solution and the convective fluxes [18]

$$u_h(\mathbf{x}, t) = \sum_j \varphi_j(\mathbf{x}) u_j(t), \qquad (\mathbf{v}u)_h(\mathbf{x}, t) = \sum_j \varphi_j(\mathbf{x})(\mathbf{v}_j u_j)(t). \tag{5}$$

The semi-discrete problem that is obtained by substituting the above expressions into the weak form (3) and replacing the test function w by φ_i can be written compactly in matrix form [8]

$$M_C \frac{\mathrm{d}u}{\mathrm{d}t} = Ku. \tag{6}$$

Here, $M_C = \{m_{ij}\}$ denotes the consistent mass matrix with coefficients $m_{ij} = \int_\Omega \varphi_i \varphi_j \, \mathrm{d}\mathbf{x}$. The entries of the discrete transport operator $K = \{k_{ij}\}$ are given by

$$k_{ij} = -\mathbf{v}_j \cdot \mathbf{c}_{ij}, \qquad \mathbf{c}_{ij} = \int_\Omega \varphi_i \nabla \varphi_j \, \mathrm{d}\mathbf{x}. \tag{7}$$

For fixed meshes, coefficients m_{ij} and $\mathbf{c}_{ij}$ do not change and need to be evaluated just once. Hence, matrix K can be assembled and, in case of an unsteady velocity field, updated in each time step in an efficient way from formula (7) without resorting to costly numerical quadrature. In particular, the efficient use of low-order finite elements [3] which require higher-order quadrature due to the presence of fourth-order terms is feasible. Additional costs are incurred for precomputing the coefficient matrices once but their repeated application in assembling system (6) is as efficient as for standard linear and bi-/trilinear low-order finite elements.

The differential algebraic equation (6) for the single unknown u_i can be cast into [19]

$$\sum_j \left[m_{ij} \frac{\mathrm{d}u_j}{\mathrm{d}t} \right] = \sum_{j \neq i} k_{ij}(u_j - u_i) + \delta_i u_i, \qquad \text{where} \quad \delta_i = \sum_j k_{ij}. \tag{8}$$

The last term in the right-hand side is an approximation of $-u\nabla \cdot \mathbf{v}$. It vanishes for divergence-free velocity fields and may engender a physical growth of solution values otherwise. The remaining 'incompressible' part of the discrete transport operator K can be assembled by summing over all edges ij connecting the i-th degree of freedom with its neighbor j. For each pair of degrees of freedom i and j there is an edge if their basis functions have overlapping support.

3   ALGEBRAIC FLUX CORRECTION

Computing approximate solutions to the pure transport problem (1) by the Galerkin method is known to produce nonphysical oscillations in the vicinity of steep gradients unless some suitable stabilization of the convective term is employed. An algebraic approach to transform the unstable high-order discretization (6) into a positivity-preserving high-resolution scheme was devised by Kuzmin [8] and refined in a series of publications [9–11, 14, 15, 17–19].

A key ingredient of algebraic flux correction is the concept of *local extremum diminishing* schemes introduced by Jameson [7]. It states that a semi-discrete scheme of the form

$$m_i \frac{\mathrm{d}u_i}{\mathrm{d}t} = \sum_{j \neq i} \sigma_{ij}(u_j - u_i) \qquad \text{for all } i \tag{9}$$

does not enhance local minima/maxima provided that $m_i > 0$ and all off-diagonal coefficients are non-negative. The above criterion is commonly violated by the high-order discretization (8). It can be enforced *a posteriori* by applying two simple post-processing steps [8, 17]:

(a) replace the consistent mass matrix M_C by its row-sum lumped counterpart

$$M_L = \{m_i\}, \qquad m_i = \sum_j m_{ij}, \qquad \text{where} \quad m_i > 0, \tag{10}$$

(b) eliminate all negative entries from the high-order transport operator K by adding a discrete diffusion operator $D = \{d_{ij}\}$. It is defined as a symmetric matrix with entries

$$d_{ij} = \max\{-k_{ij}, 0, -k_{ji}\} = d_{ji}, \qquad d_{ii} := -\sum_{j \neq i} d_{ij} \tag{11}$$

and has zero row and column sums due to the above definition of diagonal entries.

The above manipulations lead to the desired local extremum diminishing low-order scheme [17]

$$M_L \frac{\mathrm{d}u}{\mathrm{d}t} = Lu, \qquad K + D = L = \{l_{ij}\} \tag{12}$$

with all off-diagonal entries of the low-order transport operator being non-negative. It should be noted that the inequality $m_i > 0$ may not hold for all i if the consistent mass matrix has negative entries. This aspect will be addressed for non-conforming finite elements in Section 4.

The accuracy of the low-order scheme (12) is limited due to excess artificial diffusion which is applied unconditionally and does not take into account the local smoothness of the solution. The difference between approximations of high and low order (6) and (12) reads [15]

$$f(u) = (M_L - M_C)\frac{\mathrm{d}u}{\mathrm{d}t} - Du. \tag{13}$$

It is safe to add a limited amount of this antidiffusion to the low-order scheme (12) in regions where the solution is smooth. This will remove excess artificial diffusion and reduce the error introduced by the lumped mass matrix. Different limiting strategies to constrain the antidiffusive term (13) have been proposed over the years [8, 9, 11, 14, 15, 17–19]. They are based on the decomposition of the antidiffusive term (13) into sums of internodal fluxes [8, 17]

$$f_i = \sum_{j \neq i} f_{ij}, \qquad f_{ij} = \left[m_{ij} \frac{\mathrm{d}}{\mathrm{d}t} + d_{ij} \right] (u_i - u_j), \qquad f_{ji} = -f_{ij}. \tag{14}$$

The key idea is to multiply the skew-symmetric fluxes f_{ij} by symmetric correction factors

$$0 \leq \alpha_{ij} = a_{ji} \leq 1 \tag{15}$$

to compensate the excess diffusion of the low-order scheme by adding limited antidiffusion [17]

$$m_i \frac{\mathrm{d}u_i}{\mathrm{d}t} = \sum_{j \neq i} l_{ij}(u_j - u_i) + \delta_i u_i + \bar{f}_i, \qquad \bar{f}_i = \sum_{j \neq i} \alpha_{ij} f_{ij}. \tag{16}$$

It goes beyond the intention of this paper to review the various limiting strategies and explain their mathematical background. Instead, a very brief overview of the methods used to compute the numerical solutions in Section 5 is given in Appendix A. Readers interested in a comprehensive description of the algebraic flux correction paradigm including a broad collection of algorithms in pseudo code are referred to the review article [13] and the monograph [12].

4   CONFORMING AND NON-CONFORMING FINITE ELEMENTS

In this section, we present different choices for defining the set of basis functions $\{\varphi_j\}_{j=1}^{N\mathrm{dof}}$ and discuss their applicability within high-resolution schemes of AFC-type. Moreover, we address implementation issues related to special properties of non-conforming finite elements.

Let the domain $\Omega \subset \mathbb{R}^d$ be decomposed into non-overlapping convex quadrilaterals ($d = 2$) or hexahedral elements ($d = 3$) and denote the ensemble of all cells T by $\mathcal{T}_h$. A common practice in parametric finite elements is to construct the shape functions for some fixed reference element, say $\hat{T} = [-1, 1]^d$, and use the multi-linear 1-1-transformation $\Psi_T : \hat{T} \mapsto T$ given by

$$\mathbf{x} = \Psi_T(\hat{\mathbf{x}}) = B_T \hat{\mathbf{x}} + \mathbf{b}_T, \qquad B_T \in \mathbb{R}^{d \times d}, \quad \mathbf{b}_T \in \mathbb{R}^d \tag{17}$$

to transfer coordinates given in the reference frame into the physical space and vice versa. The map is unique up to a rotation in the local numbering of vertices in $\hat{T}$ and T, respectively.

Parametric finite elements for rectangular grids are given by the general expression

$$\mathcal{Q}(T) = \{q \; : \; q = \hat{q} \circ \Psi_T^{-1}, \hat{q} \in \hat{\mathcal{Q}}(\hat{T})\}, \tag{18}$$

whereby different finite elements are obtained by defining the function space $\hat{\mathcal{Q}}(\hat{T})$ accordingly.

4.1   Conforming Q_1 finite elements

A standard approach to construct low-order finite elements for quadrilaterals and hexahedral cells is to consider the space of d-linear polynoms, i.e. $\hat{Q}_1(\hat{T}) = \mathrm{span}\langle 1, \hat{x}, \hat{y}, \hat{x}\hat{y}\rangle$ in 2D, and define the four (eight in 3D) local shape function on the reference cell as tensor products of the one dimensional shape functions $\hat{\varphi}_1(\hat{x}) = \frac{1}{2}(1 - \hat{x})$ and $\hat{\varphi}_2(\hat{x}) = \frac{1}{2}(1 + \hat{x})$.

The resulting finite element basis functions φ_i exhibit the property $\varphi_i(\mathbf{x}_j) = \delta_{ij}$. That is, the i-th basis function equals one at vertex $\mathbf{x}_i$ and vanishes at all other nodes $\mathbf{x}_j \neq \mathbf{x}_i$. Moreover, its local support extends over all cells T that share the common vertex $\mathbf{x}_i$. This property implies that the number of edges ij connected to node i is proportional to the number of cells meeting at the common vertex. Figure 1 (left) illustrates the situation in two dimensions, where the number of edges equals twice the number of quadrilaterals surrounding the interior node i.

The presence of an edge ij corresponds to a non-vanishing off-diagonal coefficient in the finite element matrices (i.e. $\exists ij \Leftrightarrow m_{ij} \neq 0$). For an unstructured mesh, the number of non-zero entries may vary considerably from one row to the other especially for three-dimensional
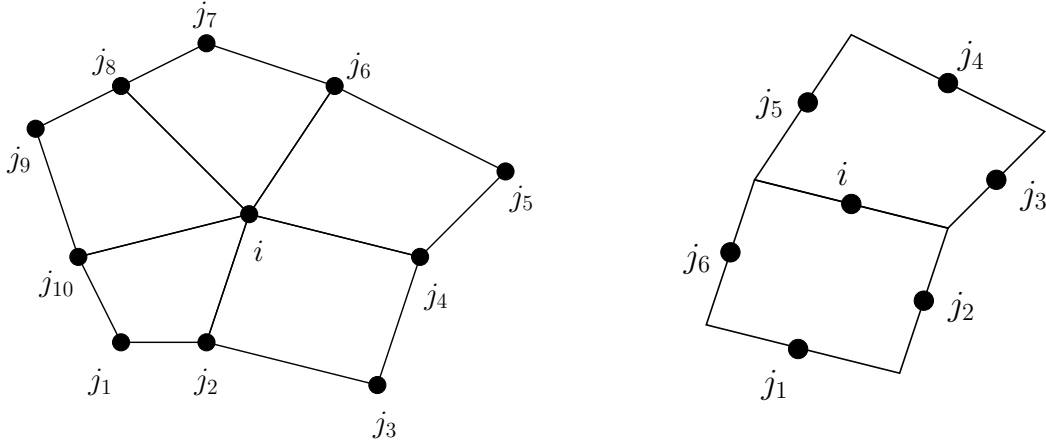
Figure 1: Connectivity between degrees of freedom for Q_1 (left) and Q_1^{rot} finite elements (right) in two dimensions.

problems. Matrices with non-uniform row length are typically stored in the CSR (compressed sparse row) or the COO (coordinate) format. Albeit utmost flexibility, general-purpose sparse matrix representations are not well-suited to achieve highest performance within sparse matrix-vector multiplications [1, 24]. Due to the lack of a regular sparsity structure, memory accesses are mostly non-coalesced which makes the implementation of optimized SpMV-algorithms for modern multi-core CPUs and many-core GPUs a challenging task. The trend in modern scientific computing is to use hybrid approaches [1] which make use of structured formats whenever possible and resort to general-purpose sparse matrix representation for exceptional matrix rows.

4.2 Non-conforming Q_1^{rot} parametric finite elements

The global continuity of Q_1 approximations across entire element boundaries can be relaxed by using non-conforming finite elements which require continuity only in the degrees of freedom. Thus, chances are high that steep fronts can be represented more accurately than with globally continuous finite elements. In fact, this is considered the strength of discontinuous Galerkin (DG) methods which give up any continuity requirement from the outset. In contrast to the latter, non-conforming *continuous* Galerkin methods do not duplicate the degrees of freedom on cell boundaries so that the total number of unknowns is smaller than for DG methods.
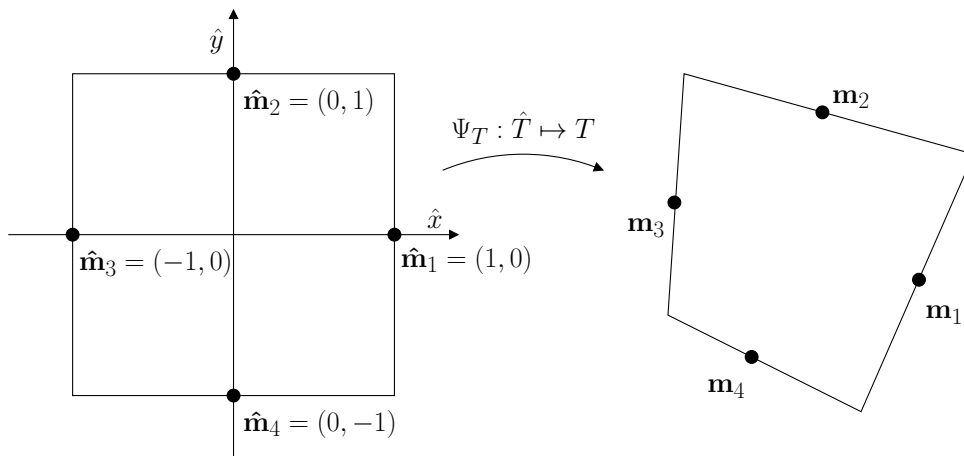

Figure 2: Rotated bilinear finite element.

6

Making use of expression (18), *rotated* bi- and trilinear shape functions are defined as [23]

$$\hat{Q}_1^{\mathrm{rot}}(\hat{T}) = \mathrm{span}\langle 1, \hat{x}, \hat{y}, \hat{x}^2 - \hat{y}^2 \rangle \qquad (d = 2) \tag{19}$$

$$\text{and} \quad \hat{Q}_1^{\mathrm{rot}}(\hat{T}) = \mathrm{span}\langle 1, \hat{x}, \hat{y}, \hat{x}^2 - \hat{y}^2, \hat{y}^2 - \hat{z}^2 \rangle \qquad (d = 3), \tag{20}$$

respectively. A natural way to define the degrees of freedom for quadrilaterals is to associate them with the edge midpoints $\hat{\mathbf{m}}_1 = (1, 0)$, $\hat{\mathbf{m}}_2 = (0, 1)$, $\hat{\mathbf{m}}_3 = (-1, 0)$, and $\hat{\mathbf{m}}_4 = (0, -1)$ of the reference rectangle $\hat{T} = [-1, 1]^2$ and define the four nodal shape functions as follows [5]

$$\hat{\varphi}_1(\hat{\mathbf{x}}) = \frac{1}{4} - \frac{1}{2}\hat{y} - \beta(\hat{x}^2 - \hat{y}^2), \tag{21}$$

$$\hat{\varphi}_2(\hat{\mathbf{x}}) = \frac{1}{4} + \frac{1}{2}\hat{x} + \beta(\hat{x}^2 - \hat{y}^2), \tag{22}$$

$$\hat{\varphi}_3(\hat{\mathbf{x}}) = \frac{1}{4} + \frac{1}{2}\hat{y} - \beta(\hat{x}^2 - \hat{y}^2), \tag{23}$$

$$\hat{\varphi}_4(\hat{\mathbf{x}}) = \frac{1}{4} - \frac{1}{2}\hat{x} + \beta(\hat{x}^2 - \hat{y}^2), \tag{24}$$

with $\beta = \frac{1}{4}$. It is easy to check that $\hat{\varphi}_i(\hat{\mathbf{m}}_j) = \delta_{ij}$ for $i, j = 1, 2, 3, 4$ which means that the approximate solution (5) features the point-wise interpolation property $u_h(\mathbf{m}_j, t) = u_j(t)$, where $\mathbf{m}_j$ denotes midpoint of the physical edge γ_j. An analog definition is available for hexahedral elements for which the degrees of freedom are associated with the midpoints of the six faces.

An alternative choice is $\beta = \frac{3}{8}$ which is obtained by constructing the local shape function such that their integral mean values along the edge $\hat{\gamma}_j$ of the reference element satisfies [23]

$$|\hat{\gamma}_j|^{-1} \int_{\hat{\gamma}_j} \hat{\varphi}_i(\hat{\mathbf{x}}) \, \mathrm{d}\gamma = \delta_{ij} \qquad \text{for} \quad i, j = 1, 2, 3, 4. \tag{25}$$

Both choices are unisolvent with $Q_1^{\mathrm{rot}}(T)$ but the use of the midpoint based variant $Q_1^{\mathrm{rot,MP}}$ within the algebraic flux correction framework is limited. Consider the element mass matrix

$$\hat{M} = \begin{pmatrix} \frac{16}{45}\beta^2 + \frac{7}{24} & -\frac{16}{45}\beta^2 + \frac{1}{8} & \frac{16}{45}\beta^2 - \frac{1}{24} & -\frac{16}{24}\beta^2 + \frac{1}{8} \\ -\frac{16}{24}\beta^2 + \frac{1}{8} & \frac{16}{45}\beta^2 + \frac{7}{24} & -\frac{16}{45}\beta^2 + \frac{1}{8} & \frac{16}{45}\beta^2 - \frac{1}{24} \\ \frac{16}{45}\beta^2 - \frac{1}{24} & -\frac{16}{24}\beta^2 + \frac{1}{8} & \frac{16}{45}\beta^2 + \frac{7}{24} & -\frac{16}{45}\beta^2 + \frac{1}{8} \\ -\frac{16}{45}\beta^2 + \frac{1}{8} & \frac{16}{45}\beta^2 - \frac{1}{24} & -\frac{16}{24}\beta^2 + \frac{1}{8} & \frac{16}{45}\beta^2 + \frac{7}{24} \end{pmatrix} \tag{26}$$

evaluated on the reference cell. Its entries are positive provided that β satisfies the inequalities

$$0.3423 \approx \frac{1}{16}\sqrt{30} < |\beta| < \frac{3}{16}\sqrt{10} \approx 0.5929. \tag{27}$$

Noteworthy, the lower bound is invariant to the shape of the quadrilateral which has been verified using the computer algebra system MAPLE. This criterion holds for the mean value based variant $Q_1^{\mathrm{rot,MV}}$, whereas the lower bound is violated by its midpoint based counterpart $Q_1^{\mathrm{rot,MP}}$.

The numerical examples given in Section 5 illustrate that the latter approach does not work satisfactory for algebraic flux correction schemes. In all benchmark computations we checked the sign of the mass matrix coefficients which are positive for the choice $\beta = \frac{3}{8}$.

4.3 Non-conforming $Q_{1,\mathrm{npar}}^{\mathrm{rot}}$ non-parametric finite elements

The fully parametric ansatz described above can be used with any convex quadrilateral and hexahedral cell but the loss of stability and approximation properties was observed on perturbed meshes, where the shape of elements may be very different from that of a parallelogram [23].

As a remedy, the authors suggest to define the reference space individually for each cell

$$Q_{1,\mathrm{npar}}^{\mathrm{rot}}(T) = \mathrm{span}\langle 1, \xi, \eta, \xi^2 - \eta^2 \rangle \qquad (d = 2) \qquad (28)$$

adopting the local coordinate system (ξ, η) which connects the midpoints of the opposite edges. The mean value based variant $Q_{1,\mathrm{npar}}^{\mathrm{rot,MV}}$ was found to be most robust on perturbed meshes [23].

4.4 Taxonomy of non-conforming finite elements

Consider the situation displayed in Figure 1 (right) for the interior degree of freedom i. It is connected to other nodes sharing the common elements by *exactly* six edges ij_k, $k = 1, \ldots, 6$. It follows that each matrix row associated with an interior unknown has seven (eleven in 3D) non-zero entries. In particular, it makes no difference whether structured or completely unstructured meshes are employed. The number of non-zero matrix coefficients in rows associated with boundary 'nodes' equals four and six in 2D and 3D, respectively. It is therefore advisable to store sparse finite element matrices in the ELLPACK format [6] which is well-suited for vector architectures [1]. Instead of supporting variable row lengths, the ELLPACK format provides space for a constant number of entries within each row and pads shorter rows with zeros. This 'simplification' makes it possible to devise very efficient SpMV-implementations optimized for many-core architectures [1, 24]. It is therefore beneficial to reorder the degrees of freedom such that interior ones and those located at the boundary are separated. Afterwards, finite element matrices can be stored in a 'composite' ELLPACK format using a fixed number of 7 (11 in 3D) and 4 (6 in 3D) entries per row associated with interior and boundary unknowns, respectively. In fact, we expect optimal performance since no space/time is wasted on zero padding.

Admittedly, one has to solve for a larger number of unknowns N_{dof} when using Q_1^{rot} finite elements instead of conforming ones. A well-known theorem which relates the number of vertices, edges and faces in a polyhedron is Euler's formula. As an example, consider a two-dimensional quadrilateral mesh without holes. Then the number of degrees of freedom satisfies

$$N_{\mathrm{dof}}(Q_1) + |\mathcal{T}_h| - 1 = N_{\mathrm{dof}}(Q_1^{\mathrm{rot}}). \qquad (29)$$

meaning that the vector of unknowns is enlarged by the number of elements denoted by $|\mathcal{T}_h|$ when switching from conforming to non-conforming elements. At the same time, the number of edges ij to be considered in the edge-based assembly loop (16) increases moderately

$$N_{\mathrm{edge}}(Q_1) = N_{\mathrm{dof}}(Q_1) + 3|\mathcal{T}_h| - 1, \qquad N_{\mathrm{edge}}(Q_1^{\mathrm{rot}}) = 6|\mathcal{T}_h|. \qquad (30)$$

A final remark is concerned with the implementation of AFC schemes in parallel. A straightforward approach to parallelizing loops over edges is to color them such that no two edges with the same color share a common endpoint [22]. In a sequential outer loop over the different colors the edges within one group are processed in parallel without running into concurrent memory accesses [21]. Seven (11 in 3D) colors suffice to partition the set of edges stemming from a non-conforming Q_1^{rot} finite element approximation both on structured and fully unstructured meshes. Due to the irregular sparsity pattern of conforming finite element matrices, the largest number of nonzero entries per row dictates the number of colors required for the partitioning.

5 NUMERICAL EXAMPLES

The two-dimensional solid body rotation benchmark [20] has a long tradition in testing the performance of numerical schemes for convection-dominated problems. The three geometric shapes depicted in Figure 3 (left) are prescribed as initial profile and rotated counterclockwise about the center of the unit square Ω. To this end, equation (1) is solved using the velocity field

$$\mathbf{v}(\mathbf{x}) = (0.5 - y, x - 0.5). \tag{31}$$

It is incompressible, so that $\delta_i u_i$ vanishes in equations (8) and (16). Consequently, the numerical solution must remain bounded by the minimum/maximum values of the initial data for all times.

Each of the three solid bodies has its own region which is given by a circle of radius $r_0 = 0.15$ centered about some point (x_0, y_0). Making use of the normalized distance function

$$r(x, y) = \sqrt{(x - x_0)^2 + (y - y_0^2)} \tag{32}$$

the initial profile can be characterized by the following analytic expressions:

a) slotted cylinder centered at $(x_0, y_0) = (0.5, 0.75)$

$$u_0(x, y) = \begin{cases} 1, & \text{if } |x - x_0| \geq 0.025 \text{ or } y \geq 0.85, \\ 0, & \text{otherwise.} \end{cases} \tag{33}$$

b) cone centered at $(x_0, y_0) = (0.5, 0.25)$

$$u_0(x, y) = 1 - r(x, y). \tag{34}$$

c) hump centered at $(x_0, y_0) = (0.25, 0.5)$

$$u_0(x, y) = 0.25[1 + \cos(\pi \min\{1, r(x, y)\})]. \tag{35}$$

In addition to the above conditions, the solution is initialized by zeros whenever $r(x, y) > 1$.

The exact solution matches the initial data u_0 after each complete revolution. Numerical solutions up to the final time $T = 2\pi$ have been computed by the following algorithms:
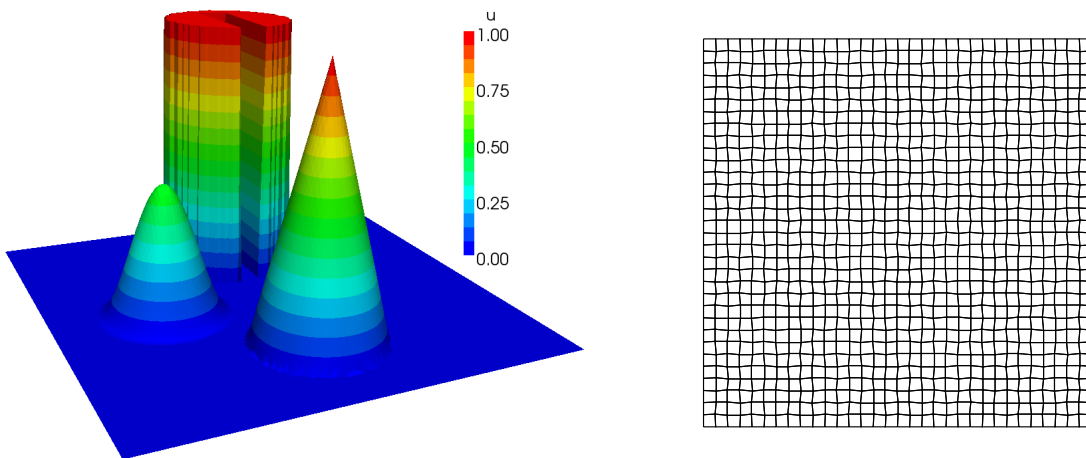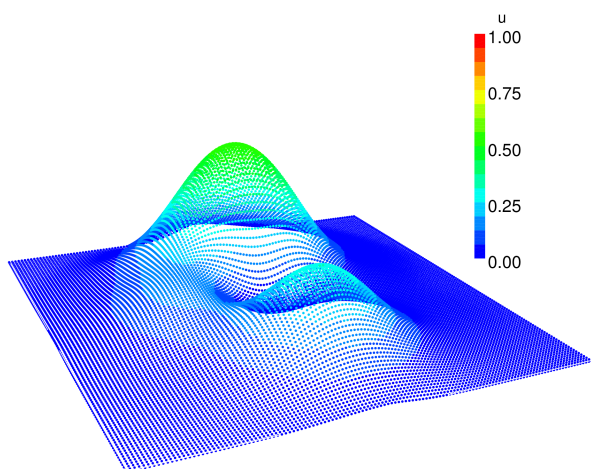

Figure 3: Solid body rotation: Initial data and exact solution at time $t = 2\pi$ (left); 5% perturbed mesh (right).

| algorithm	type of limiting	reference
low-order scheme	none	[17]
nonlinear FCT algorithm	symmetric	[17]
iterative FCT algorithm	symmetric	[14]
linearized FCT algorithm	symmetric	[11]
FEM-TVD scheme	upwind-biased	[9]

Swayed by the observations made by Rannacher and Turek for the parametric and non-parametric variants of non-conforming rotated bilinear finite elements on perturbed non-rectangular grids [23], approximations were computed on a sequence of uniform regular grids with equidistant spacing h and their non-uniform counterparts which are obtained by varying the coordinates of each internal grid point stochastically within 5% of its original position. The grid on the coarsest level is depicted in Figure 3 (right). The semi-implicit Crank-Nicolson time-stepping scheme was used keeping the ratio $\Delta t/h = 0.128$ fixed throughout all simulation runs.

Limited space forbids to display the profiles of all numerical solutions. We have decided on a selection of results which illustrate the characteristic behavior of the different approaches. All solutions displayed in this paper were computed on a grid consisting of 128×128 quadrilaterals. Figure 4 shows the 'reference' solutions which were computed by the low-order method (12) and the nonlinear FCT algorithm (37)–(38) using bilinear finite elements. The raw data at the degrees of freedom is plotted so that neither artifacts nor extra numerical diffusion are introduced by projecting the solution [16] into another, e.g., conforming space for visualization. The nonlinear FCT algorithm succeeds in resolving even the narrow bridge of the slotted cylinder reasonably well and suppresses the generation of undershoots and overshoots reliably. A well-known shortcoming of flux correction schemes – termed peak clipping – is their tendency to flatten peaks [25] which occurs at the top of the cone and the hump. On the other hand, the three shapes are smeared beyond recognition by the overly diffusive low-order method.

Next, consider the profiles shown in Figure 5 which were computed by the low-order method using Q_1^{rot} finite elements. The results are unacceptable for practical use but they give insight into the behavior of non-conforming approximations. First, smearing is slightly less pronounced as for Q_1 finite elements. The midpoint based variants begin to show their limitations for application within algebraic flux correction schemes. Their low-order profiles depicted in Figure 5

(a) low-order Q_1 solution   (b) nonlinear FCT Q_1 solution
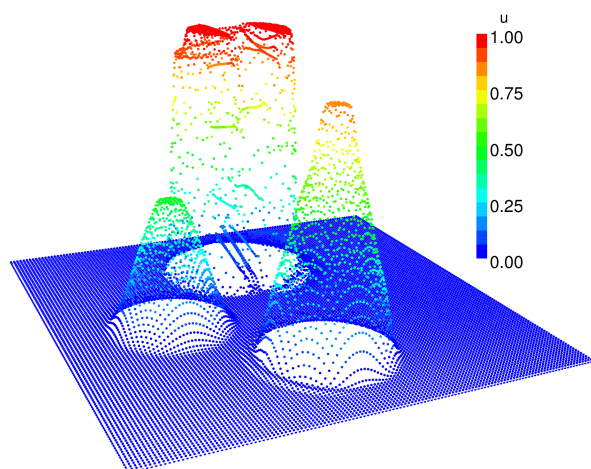
Figure 4: Solid body rotation: bilinear finite element solutions at $t = 2\pi$ on uniform mesh.

(a) $Q_1^{\mathrm{rot,MP}}$ solution, 0% perturbation
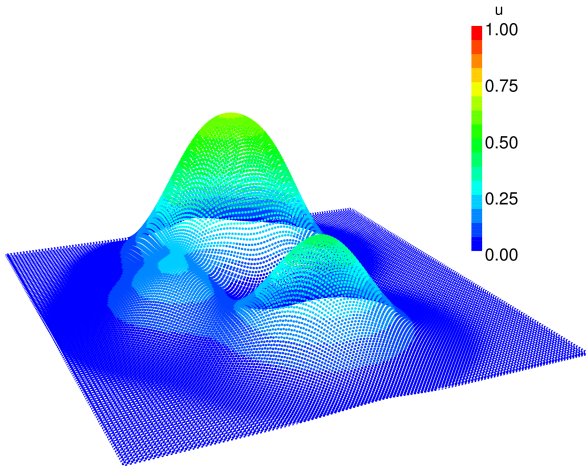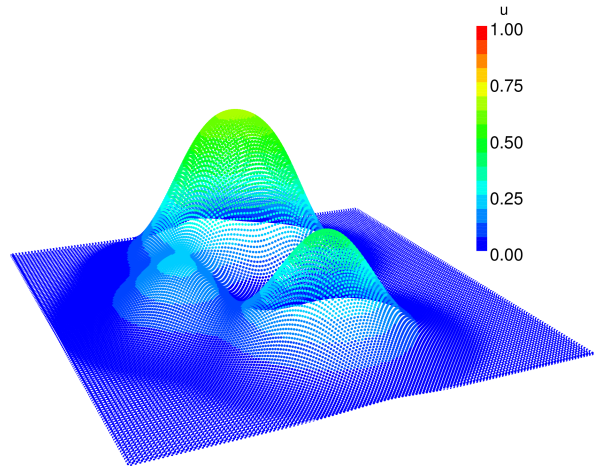
(b) $Q_1^{\mathrm{rot,MV}}$ solution, 0% perturbation

(c) $Q_1^{\mathrm{rot,MP}}$ solution, 5% perturbation
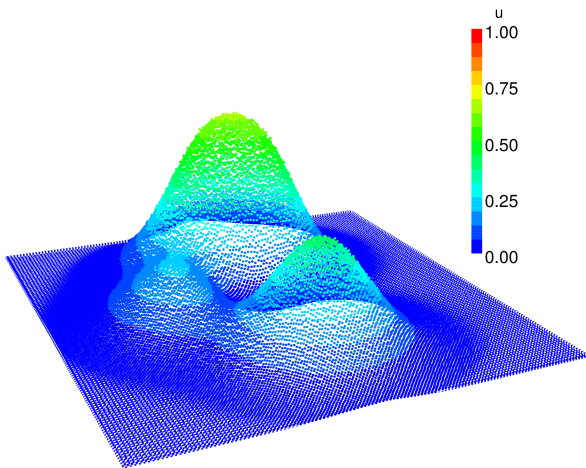
(d) $Q_1^{\mathrm{rot,MV}}$ solution, 5% perturbation
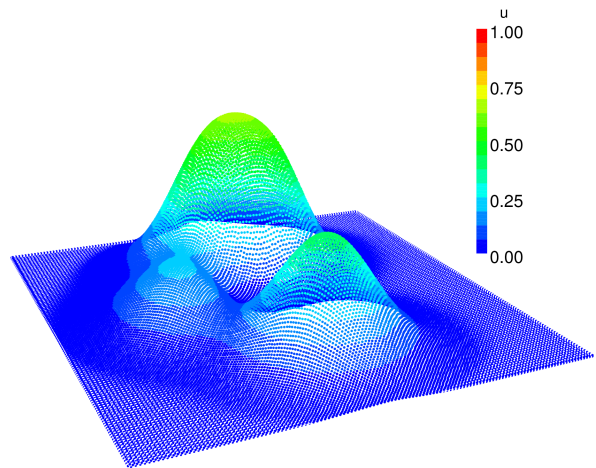
(e) $Q_{1,\mathrm{npar}}^{\mathrm{rot,MP}}$ solution, 5% perturbation
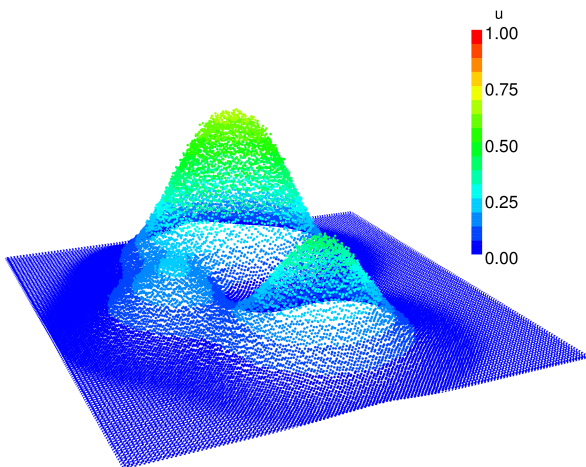
(f) $Q_{1,\mathrm{npar}}^{\mathrm{rot,MV}}$ solution, 5% perturbation
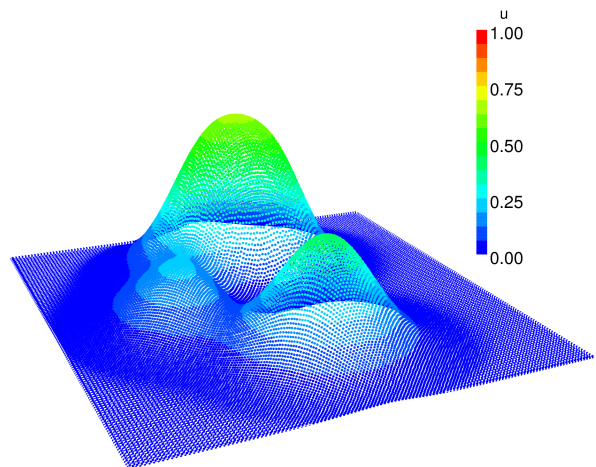
Figure 5: Solid body rotation: low-order solutions at time $t = 2\pi$ computed by non-conforming finite elements.

(a) $Q_1^{\mathrm{rot,MP}}$ solution, 0% perturbation
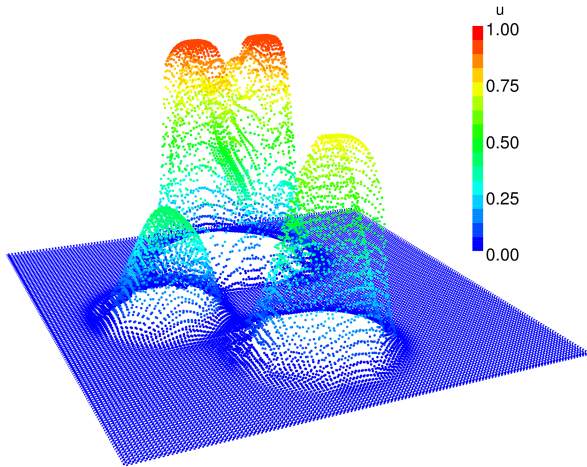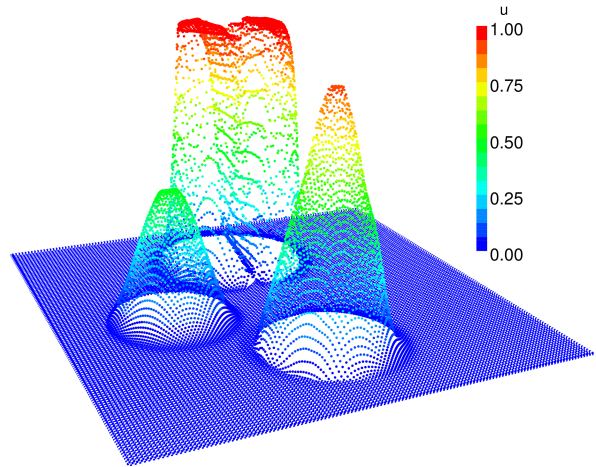
(b) $Q_1^{\mathrm{rot,MV}}$ solution, 0% perturbation

(c) $Q_1^{\mathrm{rot,MP}}$ solution, 5% perturbation
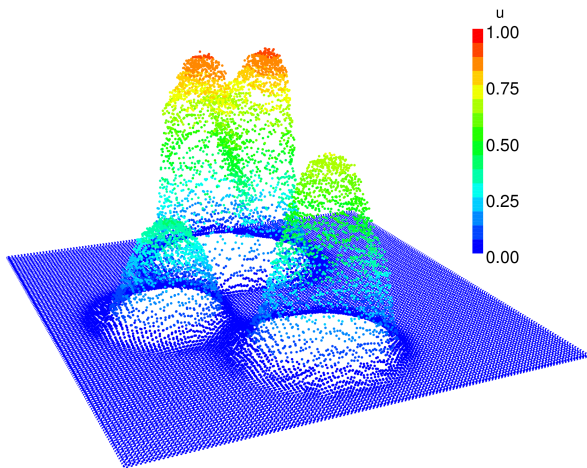
(d) $Q_1^{\mathrm{rot,MV}}$ solution, 5% perturbation
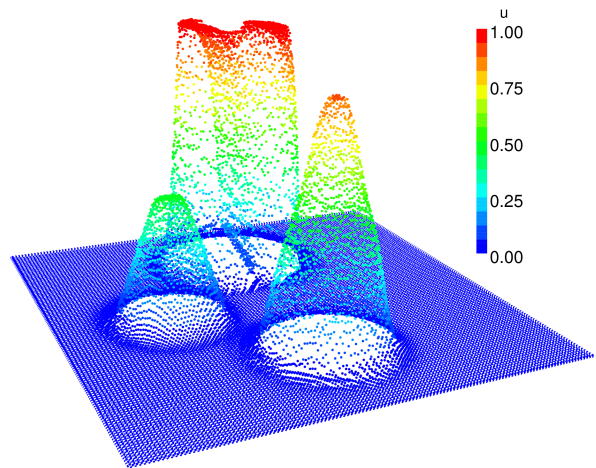
(e) $Q_{1,\mathrm{npar}}^{\mathrm{rot,MP}}$ solution, 5% perturbation
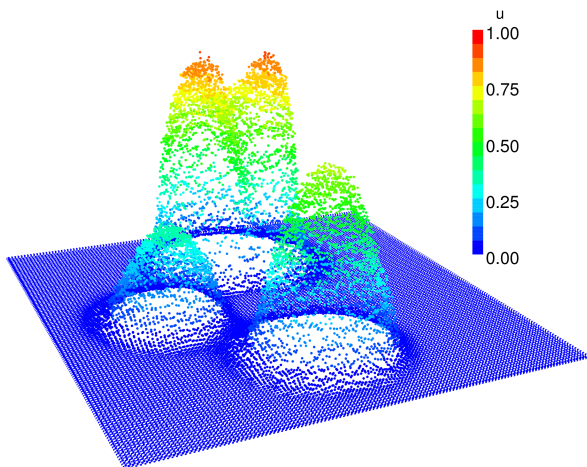
(f) $Q_{1,\mathrm{npar}}^{\mathrm{rot,MV}}$ solution, 5% perturbation
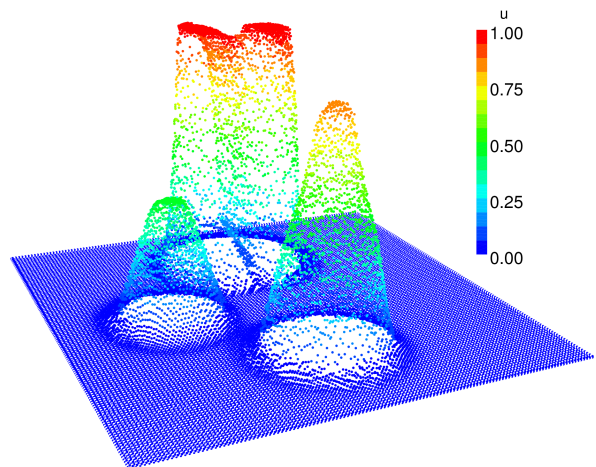
Figure 6: Solid body rotation: nonlinear FCT solutions at time $t = 2\pi$ computed by non-conforming finite elements.

(a),(c),(e) have a 'spiky look' which is most pronounced on non-rectangular grids. In contrast, the parametric and non-parametric versions of mean value based rotated bilinear elements provide a viable basis for applying flux correction; cf. Figure 5 (b),(d),(f).

The numerical results computed by the nonlinear FCT algorithm are displayed in Figure 6. As expected, the performance of the midpoint based variant is poor since the negative off-diagonal coefficients in the consistent mass matrix act as diffusive contributions to the antidiffusive fluxes (14). The resolution of steep fronts by flux corrected mean value based $Q_1^{\mathrm{rot,MV}}$ and $Q_{1,\mathrm{npar}}^{\mathrm{rot,MV}}$ finite element approximations is very crisp and free of spurious oscillations. Let us remark that peak clipping is even slightly less pronounced as for conforming approximations.

The global minimum and maximum solution values produced by different algebraic flux correction schemes are given in Table 1. Noticable erosion of the solid bodies is observed for the midpoint based variant, whereas Q_1 approximations and $Q_1^{\mathrm{rot,MV}}/Q_{1,\mathrm{npar}}^{\mathrm{rot,MV}}$ finite elements perform equally well in nearly all cases. An exception is the linearized FCT algorithm with Q_1^{rot} elements which produces profiles that exceed the upper bound by $5-6\%$. Clearly, this phenomenon needs further investigation since it also excludes non-conforming elements from being used in FCT-like constrained data projection methods [16]. By construction, the FEM-TVD scheme [9] does not make use of mass antidiffusion so that the loss of accuracy induced by mass lumping cannot be compensated by the flux limiter. It is noteworthy that non-conforming approximations preserve the maximum solution value far better then its conforming counterpart.

The convergence history of the methods is listed in Tables 2–6. In all cases, the L_2-error was computed by evaluating the integral term by high-order numerical quadrature

$$\|u - u_h\|_2 \approx \left(\sum_{T \in \mathcal{T}_h} \sum_{l=1}^{N_{\mathrm{cub}}} |u(\mathbf{x}_{l,T}, t) - \sum_j \varphi_j(\mathbf{x}_{j,T}) u_j(t)|^2 \right)^{1/2}, \tag{36}$$

where $\mathbf{x}_{l,T}$ denotes the l-th cubature point on element T. Midpoint based Q_1^{rot} elements lack convergence in most AFC schemes which precludes their further use once and for all. Comparing conforming approximations and $Q_1^{\mathrm{rot,MV}}/Q_{1,\mathrm{npar}}^{\mathrm{rot,MV}}$ elements we conclude that both approaches can be used with equal success. However, the numbers for the linearized FCT algorithm should be regarded with care since the approximate solutions are not strictly bounded.

	pert.	Q_1	midpoint based Q_1^{rot}	$Q_{1,\mathrm{npar}}^{\mathrm{rot}}$	mean value based Q_1^{rot}	$Q_{1,\mathrm{npar}}^{\mathrm{rot}}$
low-order scheme	0%	0.00 / 0.54	0.00 / 0.63	0.00 / 0.63	0.00 / 0.64	0.00 / 0.64
	5%	0.00 / 0.54	0.00 / 0.64	0.00 / 0.66	0.00 / 0.64	0.00 / 0.64
nonlinear FCT	0%	0.00 / 1.00	0.00 / 0.93	0.00 / 0.93	0.00 / 1.00	0.00 / 1.00
	5%	0.00 / 1.00	0.00 / 0.90	0.00 / 0.90	0.00 / 1.00	0.00 / 1.00
iterative FCT	0%	0.00 / 1.00	0.00 / 0.96	0.00 / 0.96	0.00 / 1.00	0.00 / 1.00
	5%	0.00 / 1.00	0.00 / 0.92	0.00 / 0.93	0.00 / 1.01	0.00 / 1.00
linearized FCT	0%	0.00 / 1.00	0.00 / 1.00	0.00 / 1.00	0.00 / 1.00	0.00 / 1.00
	5%	0.00 / 1.00	0.00 / 1.00	0.00 / 0.98	0.00 / 1.06	0.00 / 1.05
FEM-TVD	0%	0.00 / 0.79	0.00 / 0.80	0.00 / 0.80	0.00 / 0.92	0.00 / 0.92
	5%	0.00 / 0.79	0.00 / 0.74	0.00 / 0.76	0.00 / 0.92	0.00 / 0.92

Table 1: Minimum/maximum solution values computed on the $h = 1/128$ grid.

	h	Q_1	midpoint based		mean value based	
			Q_1^{rot}	$Q_{1,\text{npar}}^{\text{rot}}$	Q_1^{rot}	$Q_{1,\text{npar}}^{\text{rot}}$
0% perturbation	1/32	2.277e-01	2.165e-01	2.135e-01	2.165e-01	2.135e-01
	1/64	2.055e-01	1.950e-01	1.919e-01	1.950e-01	1.919e-01
	1/128	1.853e-01	1.725e-01	1.695e-01	1.725e-01	1.695e-01
	1/256	1.624e-01	1.497e-01	1.466e-01	1.497e-01	1.466e-01
5% perturbation	1/32	2.285e-01	2.173e-01	2.172e-01	2.145e-01	2.148e-01
	1/64	2.057e-01	1.952e-01	1.952e-01	1.924e-01	1.927e-01
	1/128	1.852e-01	1.726e-01	1.726e-01	1.698e-01	1.701e-01
	1/256	1.624e-01	1.498e-01	1.499e-01	1.470e-01	1.473e-01

Table 2: L_2 errors of the numerical solution computed by the low-order method [17].

	h	Q_1	midpoint based		mean value based	
			Q_1^{rot}	$Q_{1,\text{npar}}^{\text{rot}}$	Q_1^{rot}	$Q_{1,\text{npar}}^{\text{rot}}$
0% perturbation	1/32	1.283e-01	1.528e-01	1.528e-01	1.320e-01	1.320e-01
	1/64	8.338e-02	1.275e-01	1.275e-01	9.610e-02	9.610e-02
	1/128	5.906e-02	9.856e-02	9.856e-02	6.973e-02	6.973e-02
	1/256	4.545e-02	n.a.	n.a.	5.423e-02	5.423e-02
5% perturbation	1/32	1.288e-01	1.537e-01	1.552e-01	1.324e-01	1.323e-01
	1/64	8.379e-02	1.317e-01	1.379e-01	9.755e-02	9.795e-02
	1/128	5.920e-02	1.053e-01	1.163e-01	7.094e-02	7.075e-02
	1/256	4.536e-02	n.a.	9.854e-02	5.490e-02	5.437e-02

Table 3: L_2 errors of the numerical solution computed by the nonlinear FCT algorithm [17].

	h	Q_1	midpoint based		mean value based	
			Q_1^{rot}	$Q_{1,\text{npar}}^{\text{rot}}$	Q_1^{rot}	$Q_{1,\text{npar}}^{\text{rot}}$
0% perturbation	1/32	1.279e-01	1.486e-01	1.486e-01	1.330e-01	1.330e-01
	1/64	8.101e-02	1.210e-01	1.210e-01	9.663e-02	9.663e-02
	1/128	5.746e-02	9.110e-02	9.107e-02	6.984e-02	6.984e-02
	1/256	n.a.	n.a.	n.a.	5.444e-02	5.444e-02
5% perturbation	1/32	1.283e-01	1.495e-01	1.511e-01	1.335e-01	1.333e-01
	1/64	8.150e-02	1.255e-01	1.321e-01	9.837e-02	9.846e-02
	1/128	5.760e-02	9.805e-02	1.091e-01	7.124e-02	7.072e-02
	1/256	n.a.	n.a.	n.a.	5.519e-02	5.454e-02

Table 4: L_2 errors of the numerical solution computed by the iterative FCT algorithm [14].

6 CONCLUSIONS

This paper has shed some light on the use of non-conforming low-order finite elements within high-resolution schemes for convection-dominated problems. The algebraic flux correction paradigm was revisited in the context of rotated bi-/trilinear finite elements. In particular, the midpoint based variant $Q_1^{\text{rot,MP}}$ was shown to violate an essential design criteria. Some entries of the consistent mass matrix become negative so that row-sum mass lumping cannot be applied without hazard. Numerical solutions computed by this approach are not competitive with

	h	Q_1	midpoint based		mean value based	
			Q_1^{rot}	$Q_{1,\mathrm{npar}}^{\mathrm{rot}}$	Q_1^{rot}	$Q_{1,\mathrm{npar}}^{\mathrm{rot}}$
0% perturbation	1/32	1.514e-01	1.407e-01	1.407e-01	1.371e-01	1.371e-01
	1/64	1.202e-01	1.066e-01	1.066e-01	1.009e-01	1.009e-01
	1/128	8.421e-02	7.624e-02	7.624e-02	7.174e-02	7.174e-02
	1/256	6.226e-02	5.862e-02	5.862e-02	5.540e-02	5.540e-02
5% perturbation	1/32	1.521e-01	1.425e-01	1.439e-01	1.381e-01	1.378e-01
	1/64	1.207e-01	1.121e-01	1.224e-01	1.018e-01	1.015e-01
	1/128	8.464e-02	8.405e-02	9.801e-02	7.409e-02	7.352e-02
	1/256	6.287e-02	6.777e-02	8.319e-02	5.750e-02	5.693e-02

Table 5: L_2 errors of the numerical solution computed by the linearized FCT algorithm [11].

	h	Q_1	midpoint based		mean value based	
			Q_1^{rot}	$Q_{1,\mathrm{npar}}^{\mathrm{rot}}$	Q_1^{rot}	$Q_{1,\mathrm{npar}}^{\mathrm{rot}}$
0% perturbation	1/32	1.746e-01	1.823e-01	1.823e-01	1.542e-01	1.542e-01
	1/64	1.473e-01	1.607e-01	1.607e-01	1.297e-01	1.297e-01
	1/128	1.188e-01	1.349e-01	1.349e-01	9.713e-02	9.713e-02
	1/256	8.768e-02	1.103e-01	1.103e-01	7.139e-02	7.139e-02
5% perturbation	1/32	1.750e-01	1.840e-01	1.864e-01	1.567e-01	1.578e-01
	1/64	1.476e-01	1.633e-01	1.675e-01	1.321e-01	1.333e-01
	1/128	1.189e-01	1.419e-01	1.480e-01	1.006e-01	1.023e-01
	1/256	8.794e-02	1.209e-01	1.273e-01	7.554e-02	7.752e-02

Table 6: L_2 errors of the numerical solution computed by the FEM-TVD algorithm [9].

those obtained by standard Q_1 approximations. On the other hand, defining the local degrees of freedom in terms of integral mean values computed along edges/faces leads to non-conforming $Q_1^{\mathrm{rot,MV}}$ finite elements. Their parametric and non-parametric versions were successfully employed to compute highly accurate solutions to linear hyperbolic transport problems.

Non-conforming approximations may become more and more attractive for high performance and parallel computing. An outstanding feature is the regular sparsity pattern of finite element matrices which is preserved on fully unstructured meshes. Each matrix row has a fixed number of non-zero entries which depends only on the number of spatial dimension. It equals 7 and 4 for interior and boundary nodes in 2D, respectively. The potential of modern many-core architectures can be exploited by storing the sparse system matrices in a structured format. The gain in performance reported in [1, 24] for the ELLPACK format as compared to some general-purpose sparse matrix representations (CSR,COO) is likely to compensate for the larger number of degrees of freedom which are located at edges/faces instead of vertices. The position of unknowns is also important for designing efficient (parallel) domain decomposition methods. In essence, the unknowns at subdomain boundaries are duplicated and computed separately for each region. This implies the communication of data between processors/subdomains whenever solution values from neighboring cells are required. For non-conforming Q_1^{rot} elements communication takes place between the two cells that share a common edge/face. In contract, the communication process in vertex-based finite element schemes is more complex since the number of subdomains meeting at a vertex is not uniform in an unstructured mesh.

Further work will focus on the extension of non-conforming AFC schemes to systems of conservation laws and their efficient implementation on modern hardware platforms [21].

A APPENDIX

This appendix presents a brief overview of different limiting strategies for algebraic flux correction schemes. The interested reader is referred to [12, 13] for a comprehensive description of the mathematical background and valuable tricks and tweaks of the methods.

A.1 Nonlinear/iterative FCT algorithm

Let the semi-discrete scheme (16) be discretized in time by the two-step scheme ($0 < \theta \le 1$):

$$m_i \frac{u_i^{n+1} - u_i^n}{\Delta t} = \theta \sum_{j \ne i} l_{ij}^{n+1}(u_j^{n+1} - u_i^{n+1}) + \theta \delta_i^{n+1} u_i^{n+1} \tag{37}$$

$$+ (1 - \theta) \sum_{j \ne i} l_{ij}^n (u_j^n - u_i^n) + (1 - \theta) \delta_i^n u_i^n + \bar{f}_i. \tag{38}$$

The time derivative in the raw antidiffusive flux (14) is replaced accordingly [8, 17]:

$$f_{ij}^{\text{NLFCT}} = m_{ij} \left(\frac{u_i^{n+1} - u_i^n}{\Delta t} - \frac{u_j^{n+1} - u_j^n}{\Delta t} \right) + \theta d_{ij}^{n+1}(u_i^{n+1} - u_j^{n+1}) + (1 - \theta) d_{ij}^n (u_i^n - u_j^n). \tag{39}$$

The nonlinear system (37)–(38) is solved iteratively within a defect correction approach. In each nonlinear cycle, the antidiffusive fluxes are evaluated and constrained using formula (16). This is, where the name *nonlinear FCT algorithm* [15] comes from.

It makes use of a provisional solution which is predicted by the explicit low-order scheme

$$\tilde{u}_i = \frac{\Delta t}{m_i} \sum_{j \ne i} l_{ij}^n (u_j^n - u_i^n) + \delta_i^n u_i^n. \tag{40}$$

Zalesak's multidimensional flux limiter [25] is employed to compute a set of edge-wise correction factors α_{ij} which ensure that the converged solution to the problem (37)–(38) satisfies:

$$\min\{\tilde{u}_i, \min_{j \ne i} \tilde{u}_j\} \le u_i^{n+1} \le \max\{\tilde{u}_i, \max_{j \ne i} \tilde{u}_j\} \qquad \text{for all} \quad i. \tag{41}$$

The iterative FCT algorithm [9] adopts the above procedure with slight modifications. The amount of *accepted* antidiffusion $\bar{f}_i$ is built into the low-order predictor (40) and the correction factors α_{ij} are recomputed afterwards. However, flux correction is applied to that part of the antidiffusive fluxes which has been rejected in preceding nonlinear cycles. The aim is to build more and more antidiffusion into the end of step solution with each iteration cycle.

The repeated application of the flux limiter makes nonlinear flux correction compute-intensive. Moreover, the nonlinear iteration process may converge very slowly or stall/fail completely.

A.2 Linearized FCT algorithm

As a cost effective alternative, Kuzmin suggested to linearize the antidiffusive fluxes prior to limiting them [11]. A provisional solution $u^\star$ is computed by the low-order scheme (12) which is discretized in time by the semi-implicit Crank-Nicolson time stepping scheme

$$M_L \frac{u^\star - u^n}{\Delta t} = \frac{1}{2} (L^\star u^\star + L^n u^n). \tag{42}$$

An approximation to the time derivative $\dot{u} \approx \frac{\mathrm{d}u}{\mathrm{d}t}$ is computed from (12). Hence, we obtain

$$f_{ij}^{\mathrm{LFCT}} = m_{ij}(\dot{u}_i - \dot{u}_j) + d_{ij}^{\star}(u_i^{\star} - u_j^{\star}) \tag{43}$$

which is limited by Zalesak's limiter and applied to the fully converged low-order predictor

$$u_i^{n+1} = u_i^{\star} + \frac{\Delta t}{m_i} \sum_{j \neq i} \alpha_{ij} f_{ij}^{\mathrm{LFCT}}. \tag{44}$$

The linearized version is not as accurate as the nonlinear one but the single application of the flux limiter makes this algorithm particularly attractive for computing solutions in short time.

A.3 Upwind-biased FEM-TVD algorithm

An upwind-biased algebraic flux limiting strategy was introduced in [19] and revised in [9]. It makes use of the assumption that the edge ij is oriented such that $k_{ij} \leq k_{ji}$. That is, if the inequality is not satisfied, then the two endpoints of the directed edge $\vec{ij}$ are interchanged. The raw antidiffusive flux from node j into its 'upwind neighbor' i reads [9, 13]

$$f_{ij}^{\mathrm{TVD}} = (d_{ij} + \max\{0, k_{ji}\})(u_i - u_j). \tag{45}$$

Explicit and implicit antidiffusive fluxes are limited individually by a one-sided version of Zalesak's limiter which is valid due to the lack of the symmetric mass matrix. The FEM-TVD scheme is not well-suited for computing time accurate solutions which call for the use of compensating mass antidiffusion. Nonetheless, it is considered in our numerical study since it leads to some interesting observations for non-conforming mean value based $Q_1^{\mathrm{rot,MV}}$ finite elements.

REFERENCES

[1] N. Bell, M. Garland: Implementing sparse matrix-vector multiplication on throughput-oriented processors. In: SC '09: Proceedings of the 2009 ACM/IEEE conference on Supercomputing, 2009.

[2] M. Crouzeix. P.-A. Raviart: Conforming and nonconforming finite element methods for solving the stationary Stokes equations. *R.A.I.R.O. R3*, 7 (1973), 33–76.

[3] J. Douglas Jr., J.E. Santos, D. Sheen, X. Ye: Nonconforming Galerkin methods based on quadrilateral elements for second order elliptic problems. *ESAIM, Math. Model. Numer. Anal.* 33 (1999) 747–770.

[4] C.A.J. Fletcher: The group finite element formulation. *Comput. Methods Appl. Mech. Engrg.* 37 (1983) 225–243.

[5] I. Georgiev, J. Kraus, S. Margenov: Multilevel preconditioning of rotated bilinear non-conforming FEM problems. *Comput. Math. Appl.* 55 (2008) 2280–2294.

[6] R. Grimes, D. Kincaid, D. Young: ITPACK 2.0 Users Guide. Technical Report CNA-150, Center for Numerical Analysis, University of Texas, August 1979.

[7] A. Jameson: Computational algorithms for aerodynamic analysis and design. *Appl. Numer. Math.* 13 (1993) 33–422.

[8] D. Kuzmin: Positive finite element schemes based on the flux-corrected transport procedure. In: K. J. Bathe (ed) *Computational Fluid and Solid Mechanics*. Elsevier, 2001, 887–888.

[9] D. Kuzmin: On the design of general-purpose flux limiters for implicit FEM with a consistent mass matrix. I. Scalar convection. *J. Comp. Phys.* 219 (2006) 513–531.

[10] D. Kuzmin: On the design of algebraic flux correction schemes for quadratic finite elements. *Comput. Appl. Math.*, 218 (2008) 79–87.

[11] D. Kuzmin: Explicit and implicit FEM-FCT algorithms with flux linearization. *J. Comput. Phys.* 228 (2009) 2517–2534.

[12] D. Kuzmin: *A Guide to Numerical Methods for Transport Equations*. University Erlangen-Nuremberg, Erlangen (2010). `http://www.mathematik.uni-dortmund.de/ ~kuzmin/Transport.pdf`

[13] D. Kuzmin: Algebraic flux correction I. Scalar conservation laws. In: D. Kuzmin, R. Löhner, S. Turek (eds): *Flux-Corrected Transport: Principles, Algorithms, and Applications*. Springer, 2nd edition 2012, 145–192.

[14] D. Kuzmin, M. Möller, S. Turek: High-resolution FEM-FCT schemes for multidimensional conservation laws. *Comput. Methods Appl. Mech. Engrg.* 193 (2004) 4915–4946.

[15] D. Kuzmin, M. Möller: Algebraic flux correction I. Scalar conservation laws. In: D. Kuzmin, R. Löhner, S. Turek (eds): *Flux-Corrected Transport: Principles, Algorithms, and Applications*. Springer, 2005.

[16] D. Kuzmin, M. Möller, J.N. Shadid, M. Shashkov: Failsafe flux limiting and constrained data projections for equations of gas dynamics. *J. Comput. Phys.* 229 (2010) 8766–8779.

[17] D. Kuzmin, S. Turek: Flux correction tools for finite elements. *J. Comp. Phys.* 175 (2002) 525–558.

[18] D. Kuzmin, M. Möller, S. Turek: Multidimensional FEM-FCT schemes for arbitrary timestepping. *Int. J. Numer. Meth. Fluids* 42 (2003) 265–295.

[19] D. Kuzmin, S. Turek: High-resolution FEM-TVD schemes based on a fully multidimensional flux limiter. *J. Comp. Phys.* 198 (2004) 131–158.

[20] R.J. LeVeque: High-resolution conservative algorithms for advection in incompressible flow. *SIAM J. Numer. Anal.* 33 (1996) 627–665.

[21] M. Möller: Edge-based solvers for compressible Euler equations on multicores and GPUs. (In preparation).

[22] T. Nishizeki, N. Chiba: *Planar Graphs: Theory and Algorithms*. Annals of Discrete Mathematic 32, North Holland Mathematical Studies.

[23] R. Rannacher, S. Turek: A simple nonconforming quadrilateral Stokes element. *Numer. Meth. PDEs*, 8 (1992) 97–111.

[24] S. Williams, N. Bell, J.W. Choi, M. Garland, L. Oliker, R. Vuduc: Sparse Matrix-Vector Multiplication on Multicore and Accelerators. In: J. Kurzak, J.J. Dongarra, D.A. Bader (eds): *Scientific Computing with Multicore and Accelerators*. CRC Press (2011) 83–109.

[25] S.T. Zalesak: Fully multidimensional flux-corrected transport algorithms for fluids. *J. Comput. Phys.* 31 (1979) 335–362.